Performance Evaluation of the Valveless Micropump with Piezoelectric Actuator

Chiang-Ho Cheng

Abstract To meet the rising need in biological and medical applications, the innovative micro-electro-mechanical systems (MEMS) technologies have realized an important progress of the micropump as one of the essential fluid handling devices to deliver and control precise amounts of fluids flowing along a specific direction. This paper aims to present the design, fabrication and test of a novel piezoelectrically actuated valveless micropump. The micropump consists of a piezoelectric actuator, a vibration plate, a stainless steel chamber plate with membrane and integrated diffuser/nozzle bulge-piece design, an acrylic plate as the top cover to form the channel with the channel plate and two glass tubes for delivery liquid. The chamber and the vibration plate were made of the stainless steel manufactured using the lithography and etching process based on MEMS fabrication technology. The experimental results demonstrate that the flow rate of micropump accurately controlled by regulating the operating frequency and voltage. The flow rate of 1.59 ml/min and back pressure of 8.82 kPa are obtained when the micropump is driven with alternating sine-wave voltage of 240 V_{pp} at 400 Hz. The micropump proposed in this study provides a valuable contribution to the ongoing development of microfluidic systems.

Keywords Actuator · Diffuser · Micropump · Nozzle · Piezoelectric · Valveless

1 Introduction

Microfluidic devices, such as micropumps, play a key role in micro-electro-mechanical systems (MEMS), particularly in the fields of biological, chemical, medical, and electronics cooling [1–3]. Micropumps exploit the MEMS technology

C.-H. Cheng (✉)
Department of Mechanical and Automation Engineering, Da-Yeh University, 168, University Rd., Dacun, 51591, Changhua, Taiwan
e-mail: chcheng@mail.dyu.edu.tw

to provide the advantages including low cost, small size, low power consumption, reduction in the amount of reagents needed and small dead volume [4–6]. Various kinds of micropumping techniques have thus been developed. Nguyen et al. [7], Laser and Santiago [8], Iverson and Garimella [9] and Nabavi [10] have made the detailed reviews covering the fabrications, pumping mechanisms, actuations, valves, and operation characteristics of micropumps.

The actuation forms can be divided into two categories: mechanical and non-mechanical actuation in general. Since there are no moving elements, the structure of non-mechanical micropumps is simpler than that of mechanical micropumps. But the performance of non-mechanical micropumps are sensitive to the properties of working liquids, as discussed in the studies related to electrohydrodynamic (EHD) [11], magnetohydrodynamic (MHD) [12], electroosmotic [13] and electrochemical micropump [14]. Mechanical micropumps are relatively less sensitive to the liquid properties as compared to those non-mechanical micropumps; consequently, they may have much wider applications. The actuation mechanisms of mechanical micropumps include electrostatic [15], piezoelectric [16], electromagnetic [17], thermal pneumatic [18], bimetallic [19], shape memory alloy [20] and phase change [21] types. Due to the advantages of high stiffness, high frequency and fast response, piezoelectric actuation is very suitable to actuate micropumps especially.

In designing the vibrating displacement micropumps, a pumping chamber connected to the inlet and outlet microvalves is needed for flow rectification. Microvalves can be classified into check valve [16] and valveless [22–24] types. In check valve pumps, mechanical membranes or flaps are used with the concerned issues of wear, fatigue, and valve blocking in this type, resulting in limitation of its applications. The valveless micropumps, first introduced by Stemme and Stemme [22], implement diffuser and nozzle elements to function as a passive check valve. In addition, the peristaltic pumps or impedance pumps [4–6, 25, 26] and the Tesla-type pumps [27, 28] do not need passive check valves. The peristaltic pump consists of three chambers linked sequential. By creating peristaltic motion in these chambers, fluids can be pumped in a desired direction. Flow rectification can be also accomplished in Tesla microvalves by inducing larger pressure losses in the reverse direction compared to those in the forward direction assuming the same flow-rates. The above pump concepts have the major problems of requiring the complex design and fabrication processes. Thus, the valveless nozzle/diffuser micropumps are of particular interest for various microfluidic applications because of their simple configuration and low fabrication cost.

In order to characterize and optimize the performance of the valveless nozzle/diffuser micropumps, previous numerical and experimental studies have presented that the geometric design of the nozzle/diffuser elements can significantly affect the performance of valveless micropump. In this investigation, we proposed a high performance piezoelectric valveless micropump adopting an integrated nozzle/diffuser bulge-piece design. The micropump consisted of a stainless-steel structured chamber to strengthen its long-term reliability, low-cost production, and maximized liquid compatibility. A piezoelectric disc was also utilized to push

liquid stream under actuation. In simulating the inherently complex flow phenomena of pumping flowfield, the commercial computational fluid dynamics (CFD) software ESI-CFD ACE+$^®$ was used for numerical calculations [29].

2 Design

Figure 1 shows a novel valveless micropump proposed in this study and its cross-section view of the structure are shown in Fig. 2. The working principle of the proposed micropump is similar to that of the most contemporary valveless nozzle/diffuser micropumps. The flow is rectified owing to different pressure drops across the nozzle and the diffuser in changed flow directions. The pump cycle is divided into the supply and pump modes. During the supply model, the inlet and outlet regions operate as a diffuser and a nozzle respectively for the liquid flowing into the pump chamber. As a result, there is more fluid entering the chamber from the inlet side than that from the outlet side. Alternatively, the inlet region works as a nozzle and the outlet works as a diffuser, causing more fluid being expelled to the outlet side during the pump model. In this manner, net flow rate is generated from the inlet to the outlet. Figure 3 shows the schematic diagrams of operational principle in the supply and pump mode. In Fig. 4a, the dimensions of the etched pumping chamber were 8 mm in diameter and 70 μm in depth, respectively. Functioning as the flow-rectifying elements, the inlet width, length, height and divergence angle of the diffuser/nozzle were 800 μm, 3.1 mm, 70 μm and 10°, respectively. A 6 mm diameter and 70 μm high bulge-piece shown in Fig. 4b was right on the back side of the pumping chamber, as depicted in Fig. 4b. In this study, there were three bulge-piece diameters of 2, 4 and 6 mm at the same height tested to measure the delivered volumetric flow rates and pressures for evaluating the pumping performance in operations.
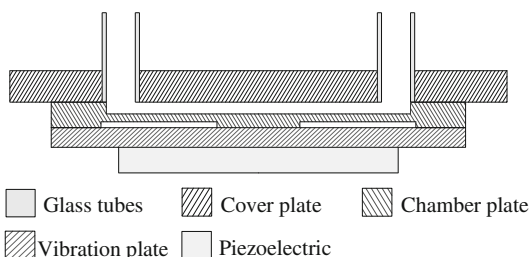
3 Fabrication

3.1 Piezoelectric Actuator

The piezoelectric disc with 200 μm thick was prepared by the commercial available piezoelectric powder (ARIOSE Company, B6 type) through the dry powder pressing technique, as illustrated in Fig. 5. The sintering process was performed in a tube furnace under a quiescent air atmosphere at a heating rate of 90 °C/min to the peak temperatures of 1,300 °C for maintaining a duration of 3 h, which followed by a 90 °C/min cooling rate to the room temperature. The poling electrodes were patterned using a screen-printing technique with silver paste. For poling the piezoelectric, the poling electric field was 2.5 V/μm under the temperature of 100 °C in 10 min.
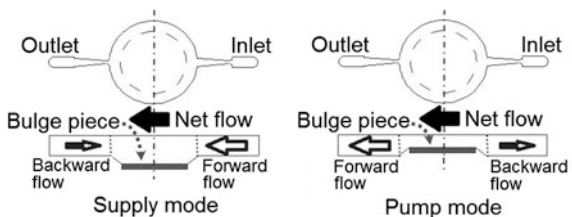
Fig. 1 Schematic of the
novel valveless micropump

Glass tubes

Cover plate

Chamber plate

Vibration plate

Piezoelectric

Top view

Bottom view
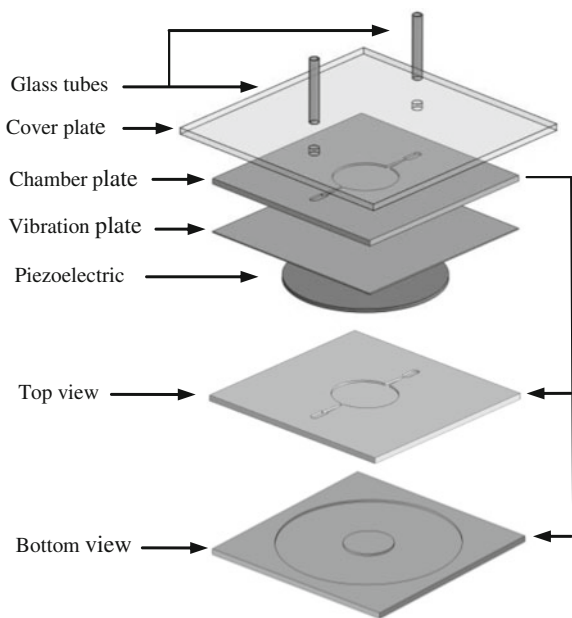
Fig. 2 The cross-section
view of micropump

☐ Glass tubes   ▨ Cover plate   ▧ Chamber plate

▨ Vibration plate   ☐ Piezoelectric

Fig. 3 The diagrams of
operational principle in
supply and pump mode

3.2 Chamber and Vibration Plate

The chamber and vibration plate were made of the stainless steel manufactured
using the MEMS-based lithography and etching process. The chamber plate mainly
included a pumping chamber (on the front side) and a bulge-piece diaphragm (on

(a) **(b)**

Unit:μm
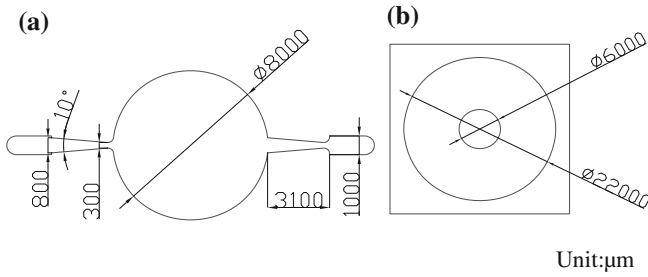
Fig. 4 The dimensions of **a** pumping chamber, and **b** bulge-piece of the micropump

Fig. 5 The fabricated
piezoelectric disc
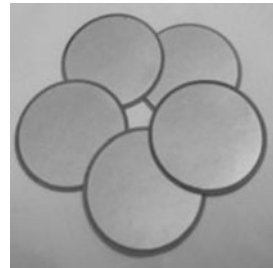
the back side) made of a stainless-steel substrate (in 25×25 mm^2) left after wet etching processes. An etchant having 46-g ferric chloride (FeCl$_3$), 33-g hydrogen peroxide (HCl) and 54-g de-ionized (DI) water was used to obtain smooth uniform flow channels on stainless-steel substrates. At the start, the AZ 9260 photoresist was coated on the stainless-steel substrate by spin coater with both spreading step and thinning step. The photoresist on the substrate was baked on a hot plate or in an oven, and then exposed by a standard UV mask aligner (Karl Suess MA-6). The UV exposure process was performed under the hard contact mode with an intensity of 6 mW/cm^2 at a wavelength of 365 nm. The exposed photoresist was then developed in an immersion process via AZ400 K diluted developer. Finally, the samples that were wet etched were immersed in the etchant at 53–58 °C. Figure 6 presents a simple overview of the major steps performed in the fabrication procedure (not to scale). Figure 7a, b illustrate the schematic diagram and pictures of a vibration and a chamber plate, respectively. The chamber plate mainly included a pumping chamber (on the front side) and a 4-mm bulge-piece diaphragm (on the back side). Figure 8 is the SEM picture of the chamber plate (close view of diffuser channel).
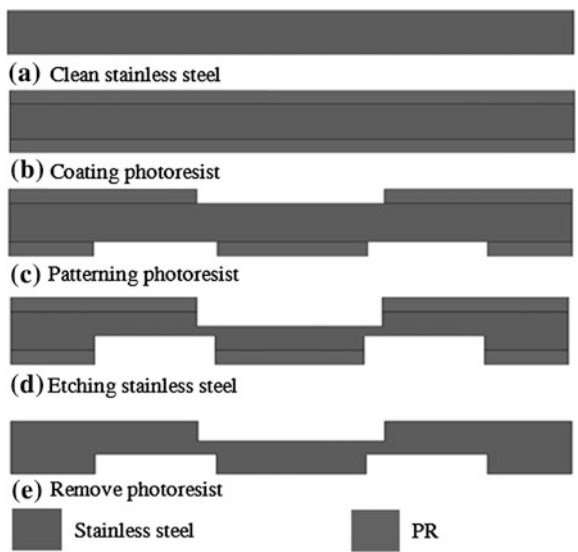
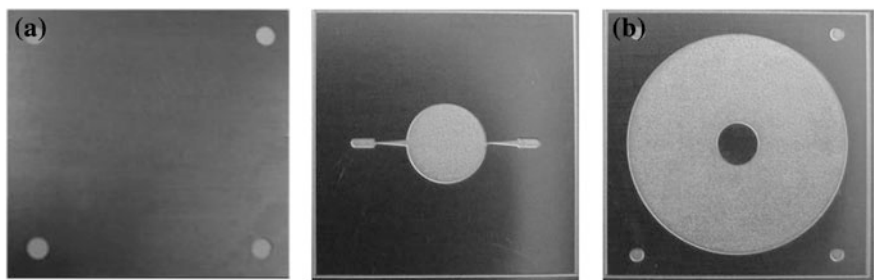**Fig. 6** Fabrication process of an etching stainless-steel micropump (not to scale)

Fig. 7 schematic diagram and pictures of **a** a vibration, and **b** a chamber plate
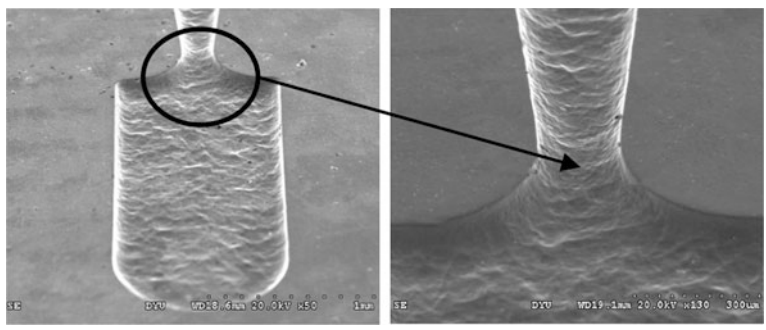

Fig. 8 SEM picture of the chamber plate (close view of diffuser channel)

3.3 Assembly

At first, applying epoxy adhesive (CIBA-GEIGY, AV 119) on the attached surfaces by screen printing, two components (chamber and vibration plate) with aligned marks were assembled by a CCD aligning system. The adhesive was cured in the oven kept at 120 °C for 2 h. Then, the piezoelectric actuator was attached by another epoxy adhesive (3 M, DP-460) cured at a lower temperature of 60 °C for 2 h to avoid depolarization. Finally, the inlet and outlet tubes were connected to the micropump inlet and outlet ports. The instant adhesive (LOCTITE, 403) was also employed to suppress permeating of epoxy adhesive into the glass tube and acrylic gap. Figure 9 shows the photo of the assembled micropump device.

4 Experimental Apparatus

The actuated displacements of the samples were measured by the 2-dimensional scanning laser vibrometer (Polytec MSV300), as displayed in Fig. 10. Each obtained data is the average value from the three measured samples with the same conditions. Figure 11 exhibits the schematic diagram of the experimental apparatus for flow rate measurements of the valveless micropump. Two silicone tubes were connected to the inlet and outlet of a micropump during the experiments. The volumetric flow rates were measured via reading the moving distance of the DI water column in the silicone tube per unit time. In the meantime, and the volumetric flow rates were determined from the mass change of the outlet reservoir [by a precision electronic balance (Precisa XS 365 M)] divided by the water density. The measurements were also conducted under various back pressures varied by lifting up the height of the downstream tube. In the tests, the piezoelectric disc was operated at the driving sinusoidal voltage of 160 V_{pp} and frequency ranging within 100–550 Hz from an electrical signal controller (Agilent 33120A function generator and Trek 50 Amplifier) with the electrical signals verified by an oscilloscope (Agilent 54622A). As the micropump was filled with DI water, gas bubble trapping was carefully eliminated to circumvent the inaccuracy in flow-rate measurements.

5 Theoretical Analysis

Simulations were conducted using the ESI-CFD ACE+$^®$ computer software to examine the internal flow field inside a micropump. The theoretical model was based on the transient, three-dimensional continuity and Navier-Stokes equations for incompressible laminar flows with a negligible temperature variation over the computational domain. The governing equations are stated as below.
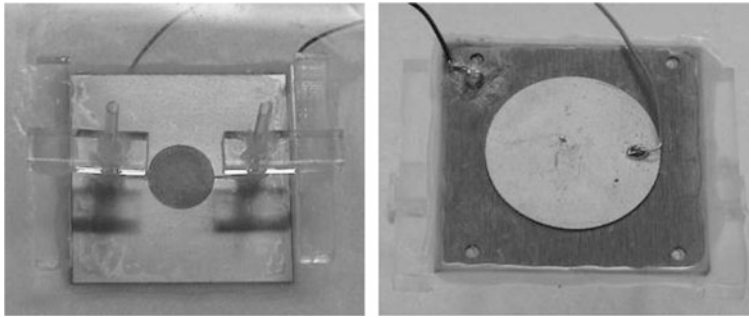
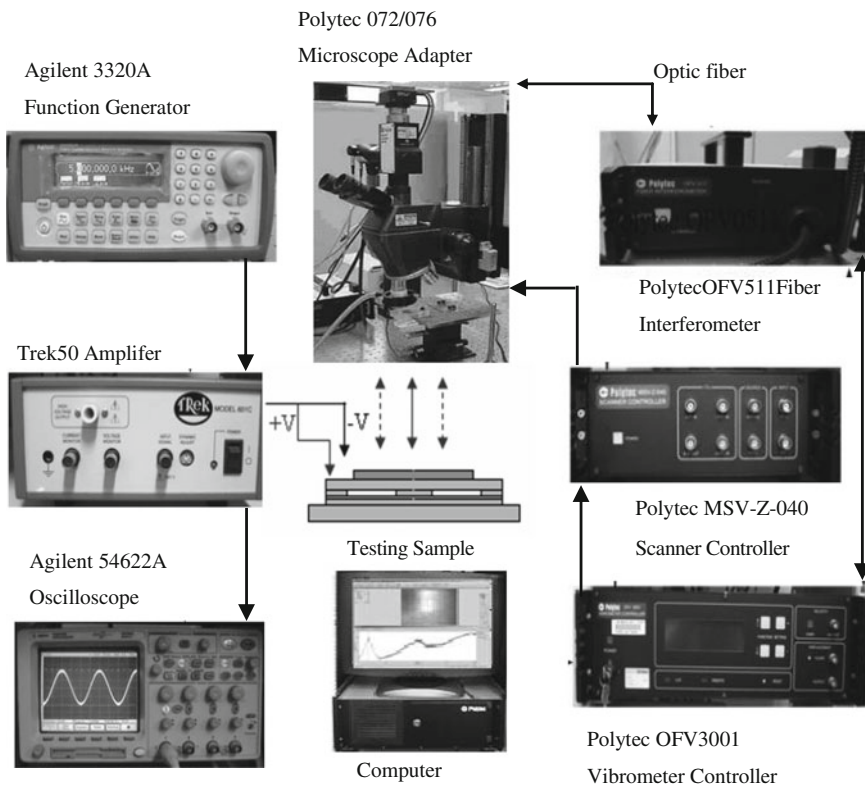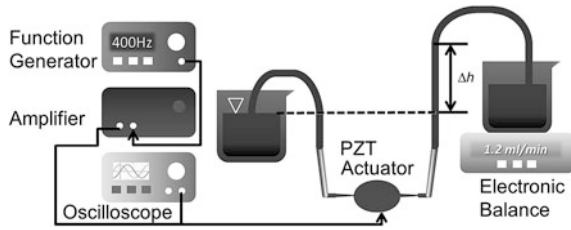**Fig. 9** The assembled valveless micropump

Fig. 10 Configuration of instruments for measuring the actuated displacement of the piezoelectric actuator

Fig. 11 Schematic diagram of the experimental setup for flow rate measurements of the micropump

$$\nabla \cdot \vec{V} = 0. \tag{1}$$

$$\frac{\partial}{\partial t}(\rho \vec{V}) + \rho(\vec{V} \cdot \nabla)\vec{V} = -\nabla p + \rho \vec{g} + \mu \nabla^2 \vec{V}. \tag{2}$$

The symbol $\vec{V}$ is the velocity vector; whereas, p, ρ and μ represent the pressure, density, and dynamic viscosity of the fluid. The term $\rho \vec{g}$ denotes the gravitational force. In this study, the ambient pressure outside the micropump was 1 atm. The no-slip condition and a zero normal pressure gradient were imposed on the solid walls of the micropump. Using the pure water as the working fluid in the experiments, the resultant values of the density and viscosity were 997 kg/m^3 and 8.55×10^{-4} N-s/m^2, respectively. The motion of the vibrating bulge-piece diaphragm was treated as the moving boundary under an applied driving voltage signal by prescribing the axial displacement on the diaphragm surface. The corresponding displacement was determined through the finite-element computer software ANSYS® to set the properties of the piezoelectric and stainless-steel materials as Young's moduli of 9.1×10^{10} and 2.13×10^{11} N/m^2, Poisson's ratios of 0.33 and 0.3, and densities of 7,900 and 7,780 kg/m^3. When considering a 6-mm-diameter and 70-μm thick bulge-piece diaphragm, a fixed boundary condition of the diaphragm was employed in the ANSYS® transient investigation for a case in which air and water were filled from two sides. The predictions showed that the displacement responded as a sinusoidal waveform having the same frequency of 400 Hz. The computed displacements were verified with the measured data from a Polytec scanning vibrometer (Polytec-MSV300®). The ANSYS® simulations and measurements indicated that the peak-to-peak amplitude of the bulge-piece diameters of 2, 4 and 6 mm at the voltage and frequency of 160 V$_{pp}$ and 400 Hz were 10.8, 10.2 and 9.8 μm (5.4/5.1/4.9 μm outward and 5.4/5.1/4.9 μm inward), respectively. The simulations were carried out using the user-defined-function (UDF) module in the ESI-CFD ACE+® software for prescribing the moving boundary of the bulge-piece diaphragm displacement and inlet/outlet boundary conditions. In calculations, the zero gauge pressure was specified at the inlet with the measured back pressure (P_b) values ranging from 0 to 5.3 kPa set at the outlet, and the volumetric flow rates were computed by averaging the cyclical volumetric flow rates over one period.

6 Results and Discussion

To simulate the flow behavior of the valveless micropump, Fig. 12 showed the numerical grids of a full-size valveless micropump model. The mesh system included three major structured portions: the pumping chamber, nozzle/diffuser, and inlet and outlet tubes. In constructing the model, finer grids were disposed in the regions near the nozzle and diffuser throats as well as the moving and fixed wall boundaries. The average cell length in the chamber was about 45.3 μm with the smallest spacing of 1.2 μm for resolving the steep variations of flow properties. Calculations were also done on the total grids of 166,672, 191,673 and 216,677 points at CFL = 0.5 and 0.25. During transient calculations, the normalized residual errors of the flow variables (u, v, w and p) converged to 10^{-5} with the mass conservation check within 0.5 % for each time step. The calculated center-line velocity profiles across the pumping chamber at different grids and CFL values indicated that satisfactory grid independence could be achieved using a mesh setup of 191,673 grids with CFL = 0.5. A complete simulation for developing a pumping flow field (with the cycle-to-cycle variation of the delivered volumetric flow rates under 0.2 %) generally requires around 140 h of central processing unit (CPU) time on an Intel-Core2 Duo E6750-2.66 GHz personal computer.

To validate the present theoretical model, numerical calculations were conducted using the ESI-CFD ACE+$^{®}$ software by comparing the predictions with experimental data. The performance of a piezoelectric valveless micropump is essentially dependent on the frequency and voltage of excitation signals for the same geometric configuration. Figure 13 illustrates the measured and computed volumetric flow rates of the bulge-piece diameters of 2, 4 and 6 mm for (a) varied frequencies from 100 to 550 Hz at a zero back pressure, and (b) different back pressures at the frequency of 400 Hz with the sinusoidal voltage of 160 V_{pp} applied. A precision electronic balance was also used to compute the volumetric flow rates from the mass variations of the outlet reservoir. Both the predictions and measurements indicate that the maximum volumetric flow rate was 1.2 ml/min at the driving frequency of 400 Hz. A decay of volumetric flow rate was observed when the input frequency was shifted away from the optimal frequency. The maximum difference between the predictions and experiment results was below 9.1 %, showing that the CFD code can simulate the pumping process of piezoelectric valveless micropumps with a reasonable accuracy. Moreover, the maximum volumetric flow rates were substantially increased by 50 and 75.1 % when the bulge-piece diameters were enlarged from 2 to 4 mm and 4 to 6 mm, respectively.

In practice, a piezoelectric valveless micropump was operated to deliver a specified level of flow rate at a desired pressure head. Figure 13b illustrates the volumetric flow rates with respect to the back pressures for the micropumps having different bulge-piece diaphragms. In the experimental process, the volumetric flow rates were measured for different back pressures varied by changing the height of
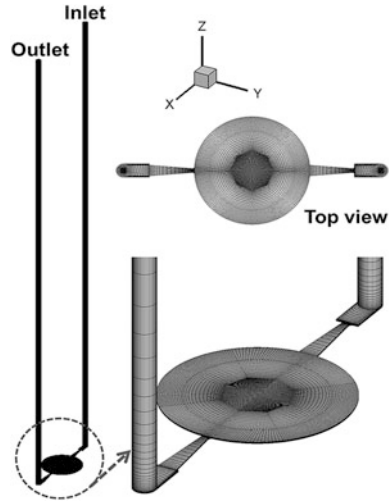
an outlet tube. The maximum pumping back pressure at a zero volumetric flow rate
was determined by directly measuring the fluid height difference between the inlet
and outlet tubes. Both the measured and simulated results showed that the volu-
metric flow rate decreased nearly linearly with the back pressure at the frequency
of 400 Hz with the sinusoidal voltage of 160 V_{pp} applied. Enlargement of the
bulge-piece diameter can essentially augment either the maximum volumetric flow
rate or the maximum back pressure. The maximum back pressures were sub-
stantially increased by 23.3 and 32.9 % when the bulge-piece diameters were
enlarged from 2 to 4 mm and 4 to 6 mm, respectively.

Figure 14 illustrates the volumetric flow rates with respect to the back pressures
for the micropumps having different voltages at 6 mm bulge-piece diaphragms.
Their pump characteristics are similar phenomenon, but their values have some
different. Figure 14 shows the volumetric flow rate gradually rises as voltages
increases in a good designed pump. The resultant maximum volumetric flow rate
and back pressure were 1.59 ml/min and 8.82 kPa for a 6-mm bulge-piece
diameter at the driving voltage and frequency of 240 V_{pp} and 400 Hz.

The position accuracy of a feed drive system was primarily influenced by the
thermal deformation of a ball screw. A high-speed ball screw system can generate
vast heat after long-term operations, with greater thermal expansion formed, and
thereby negatively impact the positioning accuracy of the feed drive mechanism.
In this research, the computational approach was applied using the FEM to sim-
ulate the thermal expansion development for solving the deformation of a ball
screw. In simulations, we implemented the multi-zone heat loads to treat the heat
generation sources from the frictions between the nut, bearings and the ball screw
shaft to emulate reciprocating movements of the nut at a top speed of 40 m/min
relative to the shaft in a time period of 3.43 s. We also employed a three-
dimensional unsteady heat conduction equation to determine the steady and time-

Fig. 13 Measured and
computed volumetric flow
rates of the bulge-piece
diameters of 2, 4 and 6 mm
for **a** varied frequencies from
100 to 550 Hz at zero back
pressure, and **b** different back
pressures at the frequency of
400 Hz with the sinusoidal
voltage of 160 V_{pp} applied
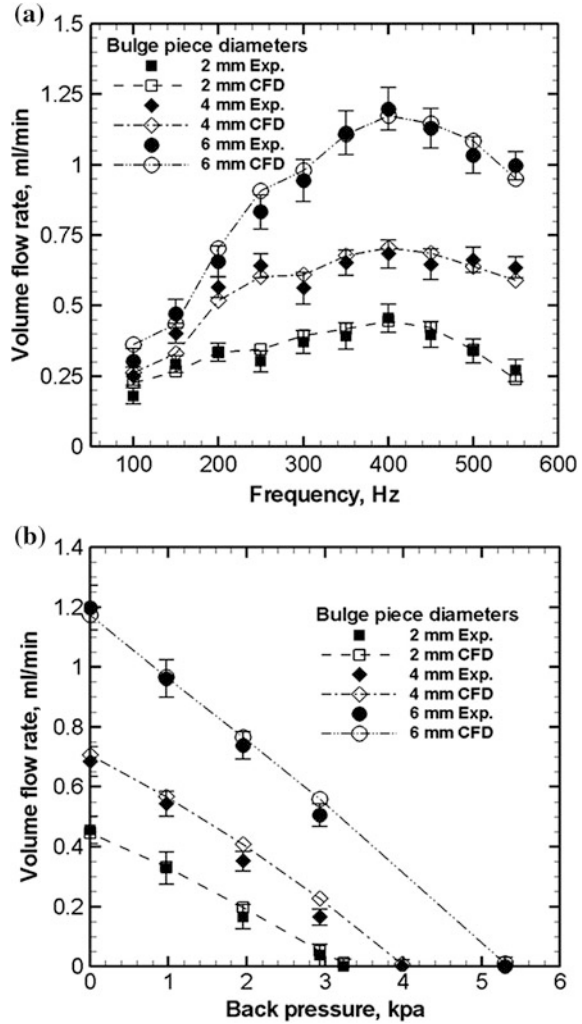
dependent temperature distributions, as well as the temperature increases for
calculating the thermal deformations of the screw shaft. Simulations were exten-
ded to consider the composite operating conditions involving various spindle
speeds and moving spans of the nut on the temperature rises and thermal defor-
mations of a ball screw shaft. Both the FEM-based simulations and measurements
found that the thermal deformations increased with the axial distance. The asso-
ciated deformations can be up to 152 μm at 0.8 m in composite operating situa-
tions, and in turn depreciated the positioning accuracy. The computational and
experimental results also indicated that the significant deterioration of the posi-
tioning accuracy due to massive heat production at high speeds of a shaft must be
thermally compensated for a ball screw system in operations.

Fig. 14 Measured and
computed volumetric flow
rates of the bulge-piece
diameters of and 6 mm for
different back pressures at the
frequency of 400 Hz with the
sinusoidal voltage of 160,
200, 240 V_{pp} applied
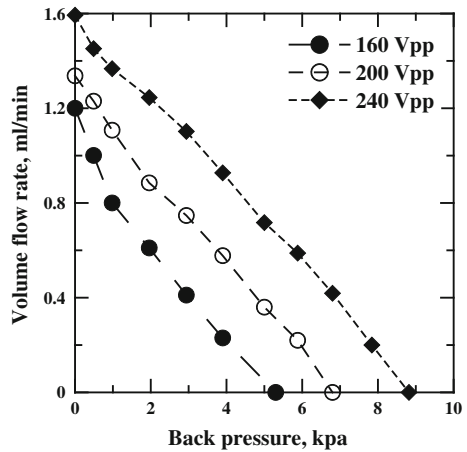
7 Conclusion

The proposed piezoelectric valveless micropump with an integrated diffuser/nozzle bulge-piece design was developed, fabricated and tested to demonstrate an effective pumping performance. The micropump consisted of a stainless-steel structured chamber to strengthen its long-term reliability, low-cost production, and maximized liquid compatibility. The resultant maximum volumetric flow rate and back pressure were 1.59 ml/min and 8.82 kPa for a 6-mm bulge-piece diameter at the driving voltage and frequency of 240 V_{pp} and 400 Hz. When the back pressure was set at 3.9 kPa, the pump could still deliver a volumetric flow rate of 0.92 ml/min. The flow pattern inside the pumping chamber was examined via numerical calculations and experimental observations. We have investigated the time-recurring flow behavior in the chamber and its relationship to the pumping performance. It was found that the micropump with the 6-mm bulge-piece diameter produced a higher suction velocity, and led to a larger upstream and downstream vortex pair during the supply phase, as compared to the outcomes for the bulge-piece diameters of 2 and 4 mm.

References

1. C. Yamahata, C. Vandevyver, F. Lacharme, P. Izewska, H. Vogel, R. Freitag, M.A.M. Gijs, Pumping of mammalian cells with a nozzle-diffuser micropump. Lab Chip **5**, 1083–1088 (2005)
2. S.S. Wang, X.Y. Huang, C. Yang, Valveless micropump with acoustically featured pumping chamber. Microfluid. Nanofluid. **8**, 549–555 (2010)

3. H.K. Ma, H.C. Su, J.Y. Wu, Study of an innovative one-sided actuating piezoelectric valveless micropump with a secondary chamber. Sens. Actuators, A **171**, 297–305 (2011)
4. L.S. Jang, W.H. Kan, Peristaltic piezoelectric micropump system for biomedical applications. Biomed. Microdevices **9**, 619–626 (2007)
5. C.Y. Lee, H.T. Chang, C.Y. Wen, A MEMS-based valveless impedance pump utilizing electromagnetic actuation. J. Micromech. Microeng. **18**, 035044 (2008)
6. Y.J. Yang, H.H. Liao, Development and characterization of thermopneumatic peristaltic micropumps. J. Micromech. Microeng. **19**, 025003 (2009)
7. N.T. Nguyen, X.Y. Huang, T.K. Chuan, MEMS-micropumps. J. Fluids. Eng. Trans. ASME **124**, 384–392 (2002)
8. D.J. Laser, J.G. Santiago, A review of micropumps. J. Micromech. Microeng. **14**, R35–R64 (2004)
9. B.D. Iverson, S.V. Garimella, Recent advances in microscale pumping technologies: a review and evaluation. Microfluid. Nanofluid. **5**, 145–174 (2008)
10. M. Nabavi, Steady and unsteady flow analysis in microdiffusers. Microfluid. Nanofluid. **7**, 599–619 (2009)
11. G. Fuhr, T. Schnelle, B. Wagner, Travelling wave-driven microfabricated electro-hydrodynamic pumps for liquids. J. Micromech. Microeng. **4**, 217–226 (1994)
12. J.C.T. Eijkel, C. Dalton, C.J. Hayden, J.P.H. Burt, A. Manz, A circular AC magnetohydrodynamic micropump for chromatographic applications. Sens. Actuators, A **92**, 215–221 (2003)
13. L. Chen, H. Wang, J. Ma, C. Wang, Y. Guan, Fabrication and characterization of a multi-stage electroosmotic pump for liquid delivery. Sens. Actuators, B **104**, 117–123 (2005)
14. J. Xie, Y.N. Miao, J. Shih, Q. He, J. Liu, Y.C. Tai, T.D. Lee, An electrochemical pumping system for on-chip gradient generation. Anal. Chem. **76**, 3756–3763 (2004)
15. M.M. Teymoori, E. Abbaspour-Sani, Design and simulation of a novel electrostatic peristaltic micromachined pump for drug delivery applications. Sens. Actuators, A **117**, 222–229 (2005)
16. G.H. Feng, F.S. Kim, Micropump based on PZT unimorph and one-way parylene valves. J. Micromech. Microeng. **14**, 429–435 (2004)
17. P. Dario, N. Croce, M.C. Carrozza, G. Varallo, A fluid handling system for a chemical microanalyzer. J. Micromech. Microeng. **6**, 95–98 (1996)
18. W.K. Schomburg, J. Vollmer, B. Bustgens, J. Fahrenberg, H. Hein, W. Menz, Microfluidic components in LIGA technique. J. Micromech. Microeng. **4**, 186–191 (1994)
19. Y. Yang, Z. Zhou, X. Ye, X. Jiang, in *Bimetallic Thermally Actuated Micropump*, vol. 59. American Society of Mechanical Engineers, Dynamic Systems and Control Division (Publication) DSC, (1996), pp. 351–354
20. E. Makino, T. Mitsuya, T. Shibata, Fabrication of TiNi shape memory micropump. Sens. Actuators, A **88**, 256–262 (2001)
21. W.Y. Sim, H.J. Yoon, O.C. Jeong, S.S. Yang, A phase change type of micropump with aluminum flap valves. J. Micromech. Microeng. **13**, 286–294 (2003)
22. E. Stemme, G. Stemme, A valve-less diffuser/nozzle based fluid pump. Sens. Actuators, A **39**, 159–167 (1993)
23. C.H. Cheng, C.K. Chen, in *WCE 2013*: *Characteristic Studies of the Piezoelectrically Actuated Valveless Micropump*. Proceedings of the World Congress on Engineering 2013. Lecture Notes in Engineering and Computer Science (London, 3–5 July 2013), pp. 1785–1790
24. B. Fan, G. Song, F. Hussain, Simulation of a piezoelectrically actuated valveless micropump. Smart Mater. Struct. **14**, 400–405 (2005)
25. L.S. Jang, Y.C. Yu, Peristaltic micropump system with piezoelectric actuators. Microsyst. Technol. **14**, 241–248 (2008)
26. J. gawa, I. Kanno, H. Kotera, T. Suzuki, Development of liquid pumping devices using vibrating microchannel walls. Sens. Actuators, A **152**, 211–218 (2009)

27. F.K. Forster, R.L. Bardell, M.A. Afromowitz, N.R. Sharma, A. Blanchard, Design, fabrication and testing of a fixed-valve micropump. IMECE FED **234**, 39–44 (1995)
28. C. Morris, F. Forster, Low-order modeling of resonance for fixed-valve micropumps based on first principles. J. Microelectromech. Syst. **12**, 325–334 (2003)
29. Y.Y. Tsui, S.L. Lu, Evaluation of the performance of a valveless micropump by CFD and lumped-system analyses. Sens. Actuators, A **148**, 138–148 (2008)